

BIOCHEMISTRY

A redox-active switch in fructosamine-3-kinases expands the regulatory repertoire of the protein kinase superfamily

Safal Shrestha¹, Samiksha Katiyar², Carlos E. Sanz-Rodriguez², Nolan R. Kemppinen², Hyun W. Kim², Renuka Kadirvelraj², Charalampos Panagos³, Neda Keyhaninejad⁴, Maxwell Colonna^{2,3}, Pradeep Chopra³, Dominic P. Byrne⁵, Geert J. Boons^{3,6}, Esther van der Knaap^{4,7,8}, Patrick A. Eyers⁵, Arthur S. Edison^{1,2,3}, Zachary A. Wood², Natarajan Kannan^{1,2*}

Aberrant regulation of metabolic kinases by altered redox homeostasis substantially contributes to aging and various diseases, such as diabetes. We found that the catalytic activity of a conserved family of fructosamine-3-kinases (FN3Ks), which are evolutionarily related to eukaryotic protein kinases, is regulated by redox-sensitive cysteine residues in the kinase domain. The crystal structure of the FN3K homolog from *Arabidopsis thaliana* revealed that it forms an unexpected strand-exchange dimer in which the ATP-binding P-loop and adjoining β strands are swapped between two chains in the dimer. This dimeric configuration is characterized by strained interchain disulfide bonds that stabilize the P-loop in an extended conformation. Mutational analysis and solution studies confirmed that the strained disulfides function as redox “switches” to reversibly regulate the activity and dimerization of FN3K. Human FN3K, which contains an equivalent P-loop Cys, was also redox sensitive, whereas ancestral bacterial FN3K homologs, which lack a P-loop Cys, were not. Furthermore, CRISPR-mediated knockout of FN3K in human liver cancer cells altered the abundance of redox metabolites, including an increase in glutathione. We propose that redox regulation evolved in FN3K homologs in response to changing cellular redox conditions. Our findings provide insights into the origin and evolution of redox regulation in the protein kinase superfamily and may open new avenues for targeting human FN3K in diabetic complications.

INTRODUCTION

Glycation is a universal posttranslational modification in which reducing sugars such as glucose and fructose are nonenzymatically added to free amine groups on peptides, proteins, and lipids. This nonenzymatic modification occurs endogenously in all living organisms, as well as exogenously in foods we consume (1, 2). Sugars attached to amine groups can undergo Amadori rearrangements to form stable linkages with biomolecules (3–5). Because such linkages can adversely affect biomolecular functions, organisms have evolved deglycation mechanisms (6–8) to repair the potentially toxic effects of reactive sugars. Fructosamine-3-kinases (FN3Ks) are a conserved family of deglycation enzymes that remove ribose and fructose sugars attached to surface-exposed lysine (Lys) residues (ketosamines) in proteins (9–12). They do this by catalyzing the transfer of the γ -phosphate from adenosine triphosphate (ATP) to the 3' hydroxyl group in the ketosamine substrate. Phosphorylation of ketosamines by FN3Ks results in an unstable ketosamine 3-phosphate intermediate, which spontaneously decomposes into inorganic phosphate (9). Because the original unmodified Lys is regenerated as a consequence

of FN3K deglycation activity, FN3Ks are believed to function as protein-repair enzymes (6, 13).

FN3Ks are conserved across the tree of life (12, 14, 15). Whereas simple eukaryotes and prokaryotes both contain a single copy of the FN3K gene, complex eukaryotes, including mammals, encode two copies, FN3K and FN3K-related protein (FN3KRP), presumably due to a gene duplication event in amphibians (14). Although the functions of FN3K homologs in lower eukaryotes and bacteria are yet to be equivocally established, it is proposed that they repair proteins modified by ribose-5-phosphate, a potent glycating agent generated by the metabolic pentose phosphate pathway (6, 12, 14, 15). FN3K activity is essential for normal cellular functions, and uncontrolled activity can result in altered cellular homeostasis and disease (16, 17). For example, accumulation of 3-deoxyglucosone, a by-product of human FN3K (HsFN3K) activity, is causatively associated with diabetic complications, such as retinopathy and neuropathy (18, 19), and the development of hepatocellular carcinoma is dependent on the deglycation of nuclear transcription factor NRF2 (encoded by nuclear factor erythroid-derived 2-like 2 gene; NFE2L2) by HsFN3K (20). Increased 3-deoxyglucosone levels also contribute to oxidative stress by inhibiting glutathione peroxidase, a potent cellular antioxidant (21). Thus, tight regulation of FN3K activity is crucial for maintaining cellular homeostasis.

We previously reported that FN3Ks belong to a large superfamily of protein kinase-like (PKL) enzymes that include eukaryotic protein kinases (ePKs), small-molecule kinases, and atypical kinases (22, 23). FN3Ks are more closely related to small-molecule kinases, such as aminoglycoside kinase/phosphotransferase (APH) and choline kinases, than ePKs and more distantly related to atypical pseudo-kinases such as Fam20C and SelO (24–26). Through quantitative comparisons of the evolutionary constraints acting on diverse PKL-fold enzymes,

¹Institute of Bioinformatics, University of Georgia, Athens, GA 30602, USA. ²Department of Biochemistry and Molecular Biology, University of Georgia, Athens, GA 30602, USA. ³Complex Carbohydrate Research Center (CCRC), University of Georgia, Athens, GA 30602, USA. ⁴Center for Applied Genetic Technologies (CAGT), University of Georgia, Athens, GA 30602, USA. ⁵Department of Biochemistry, Institute of Integrative Biology, University of Liverpool, Liverpool L69 7ZB, UK. ⁶Department of Chemical Biology and Drug Discovery, Utrecht Institute for Pharmaceutical Sciences, and Bijvoet Center for Biomolecular Research, Utrecht University, 3584 CG Utrecht, Netherlands. ⁷Department of Horticulture, University of Georgia, Athens, GA 30602, USA. ⁸Institute of Plant Breeding, Genetics and Genomics, University of Georgia, Athens, GA 30602, USA.

*Corresponding author. Email: nkannan@uga.edu

we demonstrated that ePKs share sequence and structural similarity with small-molecule kinases in the N-terminal ATP-binding lobe but diverge substantially in the C-terminal substrate-binding lobe (22, 23, 27). In particular, the extended activation segment connecting the ATP- and substrate-binding lobes that classically controls catalytic activity through conformational changes driven by reversible phosphorylation of serine, threonine, and tyrosine residues (28) is unique to ePKs and absent in small-molecule kinases, including FN3Ks (Fig. 1). A related paper from Byrne *et al.* (29) demonstrates that in addition to reversible phosphorylation, oxidation and reduction of a conserved Cys residue in the activation segment are a much more common mode of Ser/Thr protein kinase regulation than had been previously appreciated.

Here, we uncovered a critical role for the ATP-binding P-loop in the redox regulation of FN3Ks. By solving the crystal structure of a eukaryotic FN3K homolog, *Arabidopsis thaliana* FN3K (AtFN3K), we found that the P-loop is stabilized in an extended conformation by a Cys-mediated disulfide bond connecting two chains to form a covalently linked dimer in which the reduction of disulfides resulted in AtFN3K activation. Consistent with this, HsFN3K, in which the P-loop Cys is conserved, was redox-regulated and displayed altered oligomerization when proliferating cells are exposed to acute oxidative stress.

We propose that redox control mediated by the P-loop Cys is an ancient mechanism of FN3K regulation that emerged progressively during FN3K evolution from bacteria to humans. Because many protein kinases contain an equivalent redox-active cysteine in the P-loop, our studies also have broad implications for understanding the structure, function, and evolution of all PKL-fold enzymes, in particular, tyrosine kinases, which contain a cysteine residue at the equivalent position in the P-loop. Our detailed mechanistic characterization of FN3Ks also opens new avenues for the design of FN3K-targeted small-molecule inhibitors for diabetic complications associated with increased protein glycation.

RESULTS

Crystal structure of AtFN3K reveals a previously unknown strand-exchange dimer

To investigate the structural basis for biological FN3K regulation, we solved the crystal structure of a plant FN3K homolog (AtFN3K) in

complex with the ATP mimic adenylyl-imidodiphosphate (AMP-PNP) at a resolution of 2.37 Å using a multiple model molecular replacement strategy (table S1). The asymmetric unit of AtFN3K contains two molecules with a small degree of disorder at the N and C termini (residues 1 to 6 and 296 and 297) (Fig. 2A). Each chain contains a well-ordered molecule of AMP-PNP in the active site, albeit with missing electron density for γ -phosphate (Fig. 2B). AMP-PNP is known to hydrolyze slowly over time, as shown previously for protein kinase A (PKA) (30). Because the nitrogen atom in the β -phosphate of AMP-PNP could not be identified, we have modeled the ligand as adenosine diphosphate (ADP).

AtFN3K adopts a canonical PKL-fold with an N-terminal ATP-binding lobe and C-terminal substrate-binding lobe. A comparison to the bacterial search model [Protein Data Bank (PDB) code 5IGS] shows that the chains superimpose 218 C α atoms with a root mean square deviation (RMSD) of 3.3 Å (31). Because of the strong similarity between the two structures and the fact that the closely related aminoglycoside phosphotransferase structure from *Escherichia coli* (5IGS) has already been described in detail (32), we focus here on the unique structural features of AtFN3K. Unlike other kinases, the AtFN3K structure is a “strand-exchange” dimer, in which the β_1 strand in one chain forms an antiparallel β sheet with the β_2 strand of the adjacent chain (Fig. 2C). In most PKL-fold crystal structures solved to date, the β_1 strand forms an intrachain antiparallel β sheet with β_2 , and the P-loop connecting the two strands typically positions the ATP for catalysis, as observed in FN3K from *Thermobifida fusca*, aminoglycoside kinase, and the prototypic ePK PKA (Figs. 1 and 3A). However, in the AtFN3K dimer, the P-loop is unfolded, and the extended P-loop conformation is stabilized by an intermolecular disulfide bond between Cys³² in chain A and Cys³² in chain B (Figs. 2B and 3A). The electron density of the Cys³² suggests that a small fraction of the disulfides may have been cleaved by x-rays during data collection, but we could not model both conformations with confidence given the relatively low 2.4-Å resolution. A second intermolecular disulfide is formed between Cys²³⁶ in each chain (Figs. 2B and 3B). Cys²³⁶ is located in the F-G loop, which is typically involved in substrate binding in both small-molecule kinases and protein kinases (Fig. 3B). In the AtFN3K dimer, the substrate-binding lobes are covalently tethered to create a unique interface, presumably for phosphorylating ketosamine and related substrates (Fig. 3C). The AtFN3K dimer buries nearly 2500 Å² (16.4%) of solvent-accessible

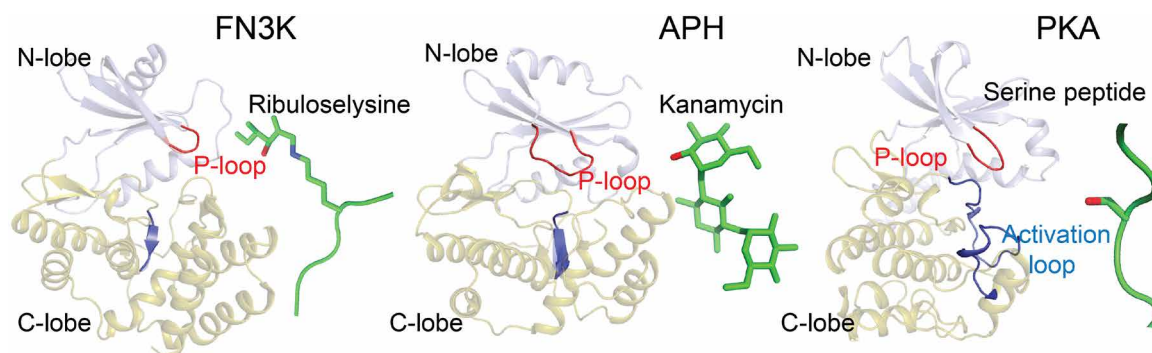


Fig. 1. FN3K adopts a protein kinase fold. Comparison of the overall fold of FN3K from *T. fusca* (TfFN3K; PDB code: 3F7W), aminoglycoside phosphotransferase (APH; PDB code: 1L8T) (85), and protein kinase A (PKA; PDB code: 1ATP) (86). The structures are shown as a cartoon where the N-lobe is colored in light blue and the C-lobe in olive green. The substrates are shown as either sticks (ribuloselysine and kanamycin) or cartoons (serine peptide) and colored green. The oxygen atom on the hydroxyl group where the phosphate group is transferred is colored in red. The P-loop and activation loop are colored in red and blue, respectively.

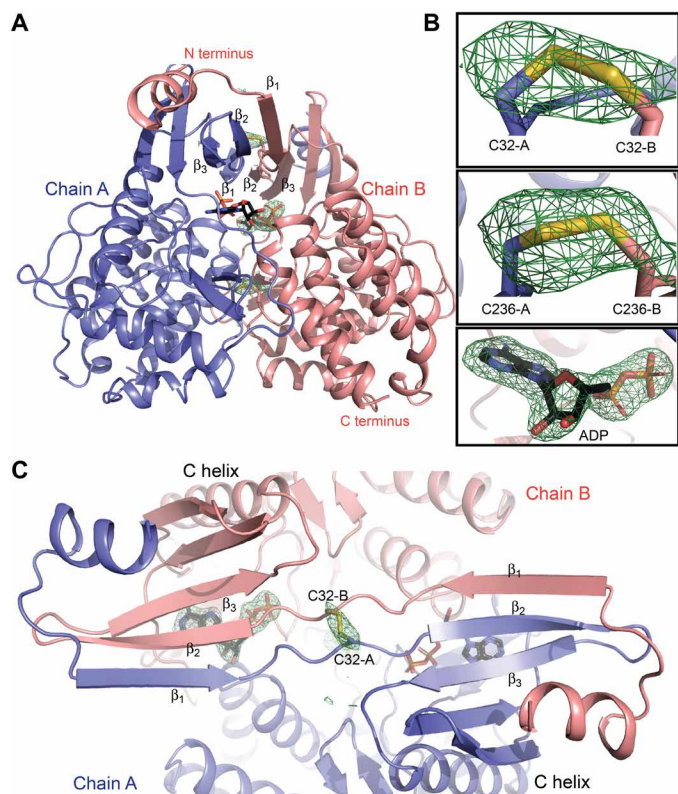


Fig. 2. WT AtFN3K is a β strand exchange disulfide-mediated dimer. (A) Cartoon representation of the crystal structure of *A. thaliana* FN3K (AtFN3K) homodimer. The two disulfide bridges between two Cys³² and two Cys²³⁶ as well as the ADP molecules are shown as sticks. (B) Simulated annealing omit difference maps ($F_o - F_c$) calculated at 2.4-Å resolution and contoured at 4.5 RMSD. Maps were calculated after substituting both cysteines with alanine (top and middle panels) and removing the ADP molecule (bottom). (C) Top view of AtFN3K showing the β strand exchange.

area of each monomer. The total solvation free energy (ΔG) gain upon dimerization is -36.2 kcal/mol, as determined by Protein Interfaces Surfaces and Assemblies (PISA) program (33), and is statistically significant ($P = 0.014$) with a total of 36 hydrogen bonds and two disulfide bridges at the dimer interface (fig. S1).

Disulfides in the AtFN3K dimer interface are conformationally strained

Disulfide bonds in proteins can be classified into various categories based on their geometry and torsional strain energy (34–36). Conformational analysis of intermolecular disulfides in AtFN3K indicates nonideal geometry (Fig. 4A). In particular, the χ_3 dihedral of -112.7° ($C\beta-S\gamma-S\gamma-C\beta$) for Cys²³⁶-Cys²³⁶ deviates from the peak distribution of $\sim 90^\circ$ observed for disulfides in the PDB (Fig. 4B). Likewise, the $C\alpha-C\alpha$ distance of 3.8 Å for Cys³²-Cys³² is much shorter than 5.7-Å peak observed for $C\alpha-C\alpha$ distances in the PDB (37, 38). These nonideal geometries suggest that the intermolecular disulfides, particularly the Cys²³⁶-Cys²³⁶ disulfide, are conformationally strained.

P-loop cysteine is critical for the formation of disulfide-linked dimer species

Next, we wanted to test whether either or both cysteines are essential for the observed disulfide-linked dimer. We mutated the cysteine residues individually and together to alanine residues and subjected

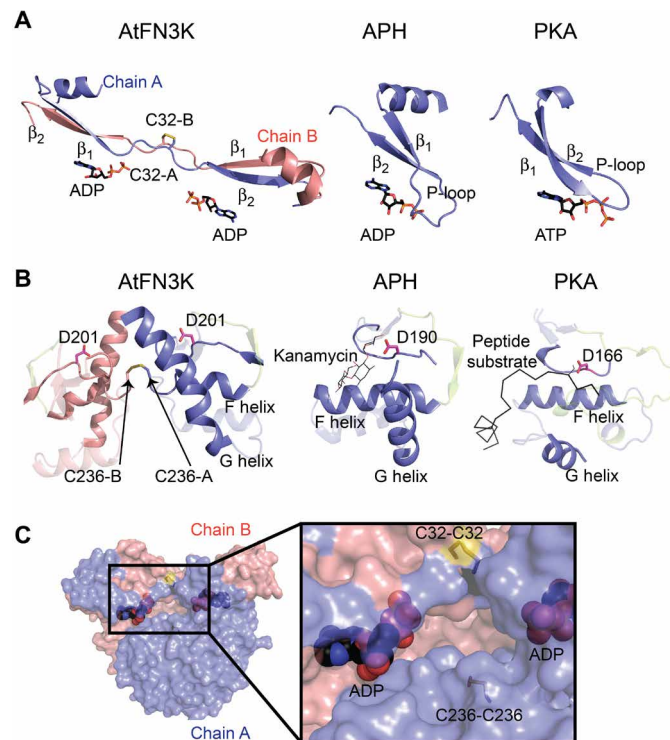


Fig. 3. Comparison of the ATP and substrate-binding regions in AtFN3K with APH and PKA. (A) Comparison of the P-loop of AtFN3K with that of APH and PKA. PDB codes 1L8T and 1ATP were used for APH and PKA, respectively. Carbon atoms of ADP and ATP molecules are colored in black, and the oxygen atoms are colored in red. Chain A and chain B of AtFN3K are colored in slate and salmon, respectively. (B) Comparison of the substrate-binding lobe of AtFN3K with APH and PKA. Catalytic aspartate is shown as sticks with carbon atoms colored in magenta. The activation loop is colored in lemon. The APH substrate kanamycin is shown as lines with carbon atoms colored in magenta. The PKA peptide substrate is shown as ribbon and colored in black. The serine residue in the peptide is modeled and shown as lines. PDB codes were used as in (A). (C) Surface representation of AtFN3K. Chain A and chain B and ADP-associated carbons are colored as described in (A). The two disulfide bridges, C32-C32 and C236-C236, are indicated with sticks with sulfur atoms colored in yellow.

them to nonreducing SDS-polyacrylamide gel electrophoresis (SDS-PAGE) analysis in the presence of redox agents, dithiothreitol (DTT), and hydrogen peroxide (H_2O_2). The disulfide-linked dimer is absent in the P-loop cysteine mutants (C32A and C32A/C236A) but not in the C236A mutant (Fig. 5A), suggesting that the P-loop cysteine is critical for the observed disulfide-linked dimer. In addition, we identified multiple monomeric species on the gel, including a reduced monomer (M_{Red}) and monomers with intramolecular disulfide (M_{S-S}) (Fig. 5A). The presence of M_{S-S} band in the double cysteine mutant led us to hypothesize that the two remaining cysteines, Cys¹⁹⁶ and Cys²²² (Fig. 5B), in the kinase domain could form intramolecular disulfides. To test whether an intramolecular disulfide is formed in solution or upon denaturation, we treated the size exclusion chromatography (SEC)-purified wild-type (WT) dimer with *N*-ethylmaleimide (NEM) before denaturation. NEM blocks free thiols and prevents their oxidation and subsequent disulfide formation (39). The absence of M_{S-S} and the presence of M_{Red} in the NEM-treated sample suggest that the M_{S-S} band is a consequence of denaturation (fig. S2). As a control, we also ran a nonreducing SDS-PAGE on the triple cysteine mutant (C32A/C236A/C196A), which is incapable of forming

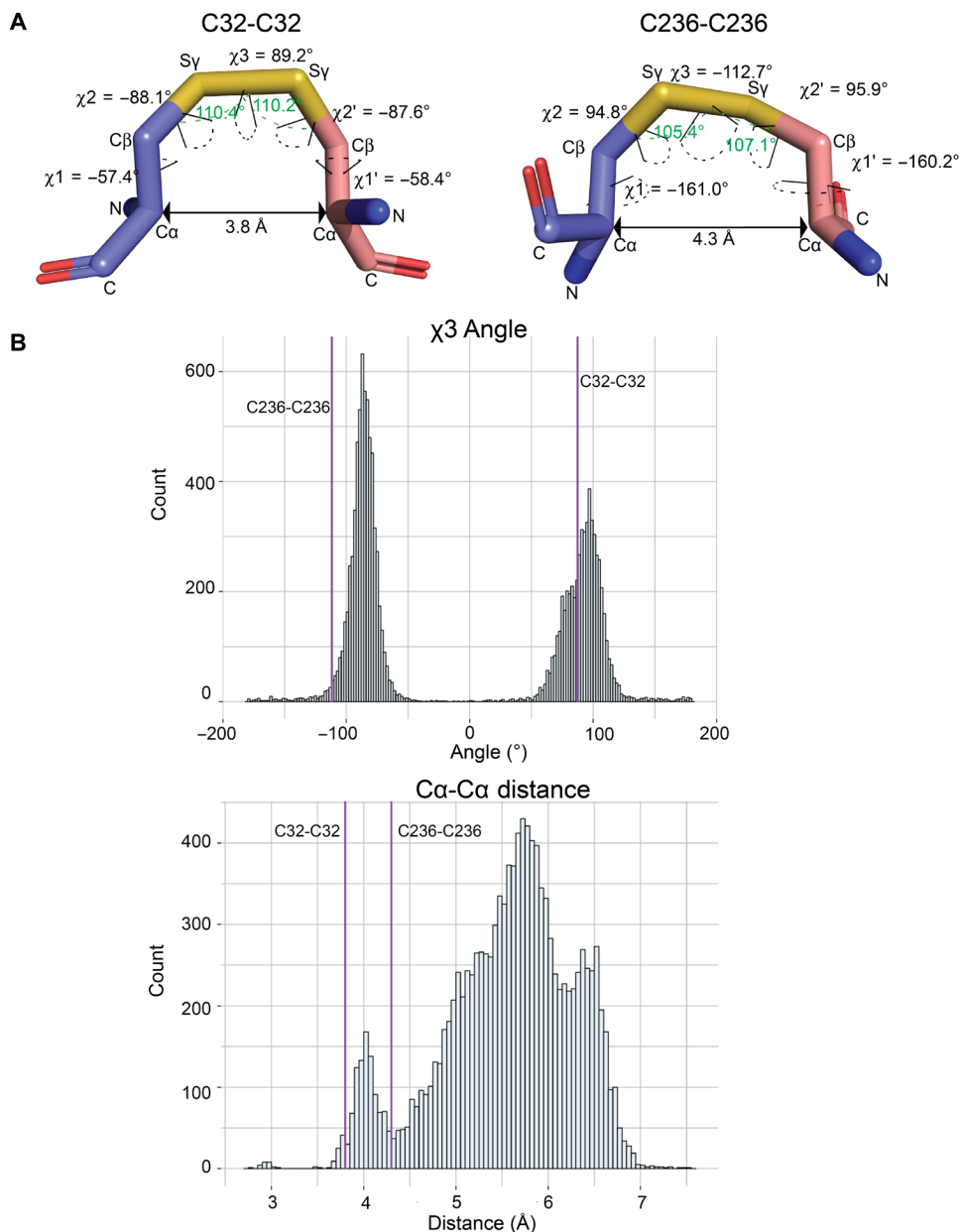


Fig. 4. Geometric analysis of the disulfides in AtFN3K. (A) Distances and dihedral values labeled for the disulfide bridges between Cys³²-Cys³² and Cys²³⁶-Cys²³⁶ between chain A and chain B. The angle (C β -S γ -S γ) is shown with a green dashed line. The dihedrals are shown with dashed line colored in black. PyMOL version 2.3 (87) was used to calculate the distances and the dihedral angles. (B) Distribution of the C α -C α distance and χ 3 angle (C β -S γ -S γ -C β) for PDB structures with a resolution of less than 1.5 Å. The data were retrieved from (64). Values for the Cys³²-Cys³² and Cys²³⁶-Cys²³⁶ disulfides in AtFN3K are represented by the purple vertical lines.

any intramolecular disulfides. As expected, only M_{Red} band was observed in the triple mutant (fig. S2), further suggesting that the M_{S-S} band is a consequence of denaturation during SDS-PAGE analysis. For this reason, we primarily focus on the interchain disulfides observed in the crystal structure.

AtFN3K WT dimer is activated by redox agents

To determine the functional state of the native enzyme (WT) in solution, we performed SEC on the purified protein. We identified

two peaks, a dimer and a monomer (Fig. 6A and fig. S3A) with the dimer peak being dominant in solution. Compared to a reducing SDS-PAGE, the purified dimer resolved on nonreducing SDS-PAGE gel as two distinct bands (fig. S4, A and B). To test sensitivity to DTT, we performed a pyruvate kinase/lactate dehydrogenase (PK/LDH) assay on the dimer and monomer fractions in the presence and absence of 2 mM DTT. The activity of the dimer species increased nearly 40-fold in the presence of the reductant (Fig. 6B). In contrast, the monomer species was active but insensitive to DTT (Fig. 6B), suggesting that only the dimer species is redox sensitive. The activity of the dimer species increased with increasing concentration of reduced glutathione (GSH), a physiological reductant (fig. S5A). We also performed PK/LDH assays on single and double cysteine to alanine or serine mutants. P-loop cysteine (C32A or C32S) mutants were less sensitive to DTT compared to C-lobe cysteine mutants (C236A/C236S) (fig. S5B). Moreover, AtFN3K WT also showed sensitivity to DTT when activity was measured independently using nuclear magnetic resonance (NMR)-based assay, which measures ribuloselysine phosphorylation (fig. S5C).

To test whether AtFN3K could dimerize without the cysteines, we performed SEC on the triple cysteine mutant (C32A/C236A/C196A). Similar to the native enzyme, we identified both dimer and monomer peaks (Fig. 6C). We hypothesized that the two species (monomer and dimer) would be insensitive to DTT because they are incapable of forming disulfide bridge. As expected, both the dimer and monomer species were insensitive to DTT (Fig. 6D). Together, these data suggest that AtFN3K can still dimerize in the absence of two cysteine residues (Cys³² and Cys²³⁶), which lie at the dimer interface.

To test whether the monomer and dimer species were in equilibrium, we first performed sedimentation velocity analysis on the purified C32A/C236A/

C196A triple mutant. *c(s)* analysis revealed a distribution consisting of a monomer peak at 2.0 S and a dimer peak at 3.1 S, which are predicted to be at 2.2 and 3.6 S, respectively (fig. S3B). Glycerol is required to maintain the recombinant AtFN3K stably in solution and tends to form a self-gradient during centrifugation, which will disproportionately reduce the S values of sedimenting species. The monomer-dimer distribution is consistent with the size exclusion profile, suggesting that the protein exists in two predominant species (Fig. 6C and fig. S3A). Next, we performed sedimentation velocity

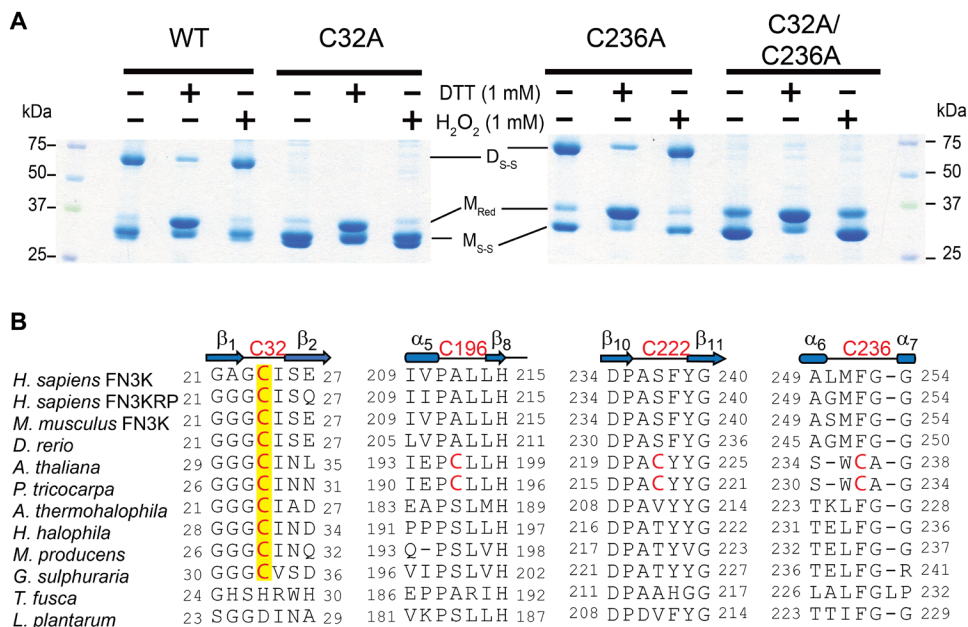


Fig. 5. P-loop cysteine of AtFN3K (Cys³²) is critical for the formation of disulfide-linked dimer species. (A) Nonreducing SDS-PAGE of WT and Cys-to-Ala mutant AtFN3K. Fifteen micrograms of protein was incubated with 1 mM DTT or 1 mM H₂O₂ for 20 min and then subjected to SDS-PAGE under nonreducing conditions. D_{S-S}, disulfide-linked dimer; M_{Red}, monomer reduced; M_{S-S}, monomer with intramolecular disulfide. Blots are representative of three experiments. (B) Multiple sequence alignment of FN3K orthologs. Two additional cysteines (Cys¹⁹⁶ and Cys²²²) specific to plant FN3Ks are shown. The alignment was generated using MUSCLE (67).

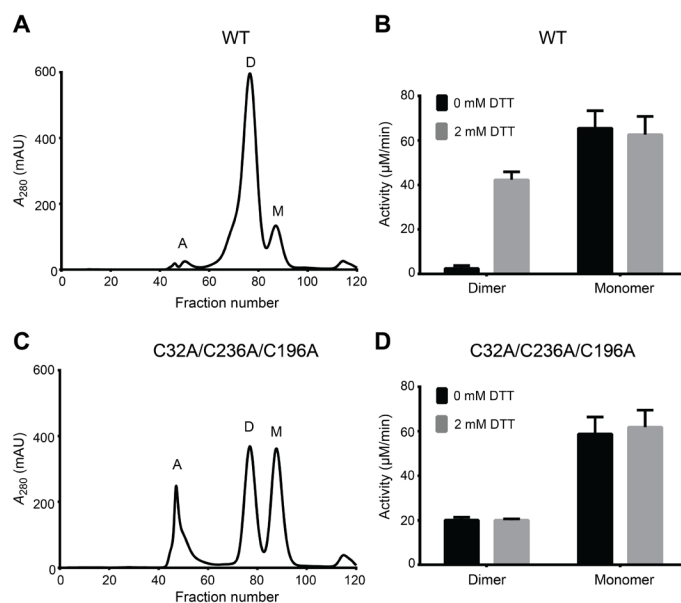


Fig. 6. Both WT and triple cysteine mutant (C32A/C236A/C196A) AtFN3K exist as two distinct species in solution, and the WT dimer is redox sensitive. (A) Size exclusion chromatography (SEC) of AtFN3K WT protein. Each fraction was 1 ml in volume. A, aggregates; D, dimer; M, monomer; A₂₈₀, absorbance at 280 nm. (B) PK/LDH assay using 1 μg of protein to assess the activity of WT protein in the presence or absence of 2 mM DTT. Ribulose-N-α-Ac-lysine was used as the substrate. Data are means ± SE of six independent experiments. (C and D) As in (A) and (B), respectively, for the triple cysteine mutant protein.

analysis across a moderate change (5×) in protein concentration but did not detect any changes in the ratio of monomers and dimers present (fig. S3B). To confirm that the species are not exchanging to any significant extent, we purified the dimer and monomer species using SEC and repeated the sedimentation velocity analysis (fig. S3C). The c(s) distribution of the purified dimer shows no significant dissociation but does contain a 1.3-S species that may correspond to a small amount of misfolded monomer. The c(s) distribution of the purified monomer suggests only a small amount of aggregation, as evidenced by a slight tailing of the c(s) peak toward larger S values (fig. S3C).

P-loop cysteine confers redox sensitivity in plant and mammalian FN3Ks

AtFN3K contains a chloroplast signal peptide N terminus of the kinase domain, and removal of the signal peptide results in the localization of AtFN3K in different cellular compartments, including nucleus and mitochondria (fig. S8). Unlike AtFN3K, other orthologs only contain the kinase domain. Multiple sequence alignment of FN3K orthologs

from diverse organisms indicates that whereas the P-loop cysteine (Cys³²) is conserved across diverse organisms, the other three cysteines (Cys²³⁶, Cys¹⁹⁶, and Cys²²²) are unique to plant FN3Ks (Fig. 5B). HsFN3K and human FN3KRP (HsFN3KRP) both contain an equivalent cysteine in the P-loop. We note that some protein tyrosine kinases that are distantly related to FN3Ks also conserve a Cys residue at the Cys³² equivalent position in the P-loop (fig. S9).

HsFN3K contains three additional cysteines, two of which are also present in HsFN3KRP. We expressed and purified HsFN3K and assayed its activity under reducing conditions. The activity of HsFN3K increased in the presence of DTT as observed for AtFN3K (Fig. 7A). Mutating the equivalent P-loop cysteine (Cys²⁴) to alanine results in loss of sensitivity to DTT. We also tested the activity in the presence of GSH. The activity increased for the WT, whereas no change was observed for the C24A mutant (fig. S6A). As a control, we expressed, purified, and assayed AtFN3K homologs from TfFN3K and *Lactobacillus plantarum* (LpFN3K), which contain a histidine and aspartate in place of the P-loop cysteine, respectively (Fig. 5B). TfFN3K and LpFN3K catalytic activity did not change in the presence of any of the redox agents tested (Fig. 7B). In addition, nonreducing SDS-PAGE for the WT and C24A HsFN3K confirmed that the P-loop cysteine is essential for dimerization (fig. S6B).

To extend these findings in mammalian cells, we expressed Flag-tagged HsFN3K in human embryonic kidney (HEK) 293T cells using transient transfection. Cells were grown for 48 hours and treated with different concentrations of diamide. Diamide decreases the cellular concentration of GSH and promotes disulfide formation (40). It can also react with free thiols in proteins and lead to disulfide bond formation (41). Diamide treatment induced dimerization and higher-order

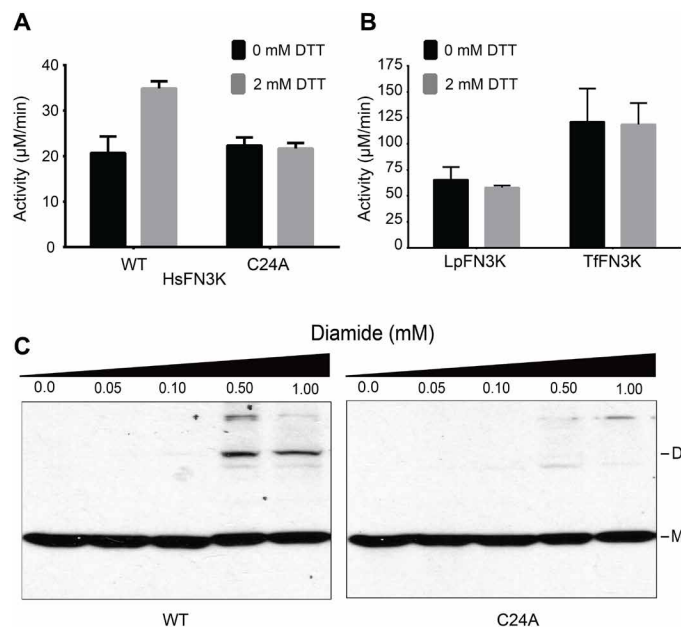


Fig. 7. P-loop cysteine contributes to redox sensitivity in HsFN3K. (A and B) PK/LDH assays performed with 10.0 μg of HsFN3K (A) or 1.0 μg each of TfFN3K and *L. plantarum* FN3K (LpFN3K) (B). Proteins were incubated with buffer (0 mM DTT) or 2 mM DTT, and ribulose-*N*- α -Ac-lysine was used as the substrate. Data are means \pm SE of three independent experiments. (C) Effect of different diamide concentrations on transfected Flag-tagged WT and C24A HsFN3K in HEK 293 cells. Total cell lysates were immunoblotted for Flag. Blot is representative of three experiments.

oligomerization of WT HsFN3K but not for C24A mutant (Fig. 7C), suggesting that the P-loop cysteine confers redox sensitivity in both plant and mammalian FN3Ks.

FN3K CRISPR knockout alters redox-sensitive cellular metabolites

Cellular functions of FN3Ks are currently unknown. Our analysis of FN3K expression in various cancer cell lines identified significant overexpression in the liver and eye cancer cells (fig. S10). To assess the functional significance of this increased expression, we generated a clustered regularly interspaced short palindromic repeats (CRISPR) knockout of HsFN3K (FN3K-KO) in the HepG2 liver cancer cell line (fig. S7) and compared the metabolome of WT and FN3K-KO cells using untargeted ^1H NMR metabolomics. This revealed a significant difference in metabolite abundance in FN3K-KO compared to WT (Fig. 8, A and B, and table S2). Glutathione and lactate levels were increased in FN3K-KO cells relative to WT HepG2 cells, whereas pantothenate, phosphocreatine/creatine ratio, aspartate, glycine, and serine levels were decreased. Glutathione is a major cellular redox regulator (42), whereas intracellular levels of pantothenate, glycine, serine, and aspartate are known to be reactive to the redox status of the cell (43–45). In addition, the phosphocreatine/creatine ratio and lactate each control ATP production and glycolysis, respectively (46). The enrichment of these metabolites suggests potential links between FN3Ks, redox levels, and ATP production.

DISCUSSION

Here, we report the structural basis for redox regulation in an ancient family of phosphorylation-based enzymes associated with

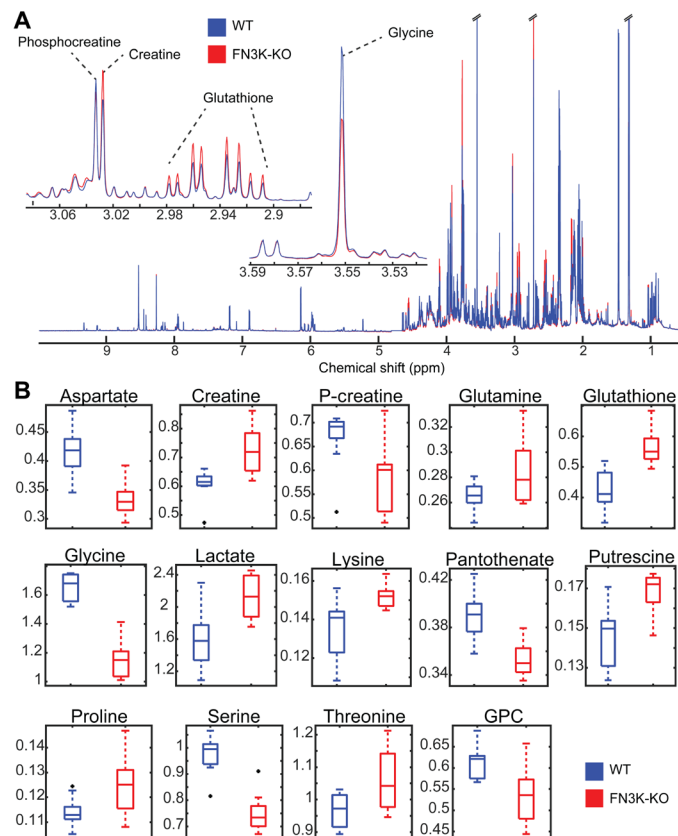


Fig. 8. Redox-sensitive metabolites are altered in HsFN3K knockout cells. (A) ^1H NMR spectra of WT and FN3K knockout (FN3K-KO) HepG2 cells. Traces are the average for each group (WT, $n = 10$; FN3K-KO, $n = 9$). Insets highlight examples of regions containing annotated metabolites observed to be significantly different between cell lines. (B) Box and whisker plots of significant (false discovery rate, $P < 0.05$) metabolites annotated with highest confidence. Black points indicate outliers. Two-tailed t test was performed, and the P values were corrected for false discovery rate using the Benjamini-Hochberg method.

protein repair. The crystal structure of AtFN3K revealed a previously unknown strand-exchange dimer in which two chains are covalently linked by disulfide bonds emanating from the P-loop in the ATP-binding lobe and F-G loop in the substrate-binding lobe. We propose that these disulfide bridges are conformationally strained and are essential for maintaining AtFN3K in an inhibited dimeric conformation. Our studies also show that inhibited native AtFN3K (WT dimer) is activated more than 40-fold under reducing conditions. We speculate that reduction of the disulfides releases the constraint on the P-loop and the substrate-binding F-G loop to allow ATP and substrate access and catalysis in the dimeric state. Thus, AtFN3K toggles between an inhibited “oxidized” dimer state and active “reduced” dimer to phosphorylate ketosamine substrates. Using SEC, we also identified a monomeric species insensitive to DTT. Although crystallization attempts to isolate the monomeric species have been unsuccessful, we predict that a monomer would adopt a canonical kinase fold without any β strand exchange. As a result, both P-loop and substrate-binding loops cannot be constrained through disulfide bridges, preventing redox regulation.

Similarly, SEC applied to the C32A/C236A/C196A mutant revealed the presence of both dimeric and monomeric species, indicating that the enzyme can dimerize without these cysteines. PISA

analysis of the crystal structure shows that nearly 2500 Å² (16.4%) of each monomer is buried as part of the dimer interface. Sedimentation velocity analysis further revealed that the two species were distinct and do not exist in equilibrium.

Our cellular studies show that dimerization and higher-order oligomerization of HsFN3K are altered after exposure to the thiol-oxidizing agent, diamide. Consistently, an unbiased proteomic study identified a sulfenylated form of the P-loop cysteine in HsFN3KRP in HeLa cells (47). Moreover, a recent proteomic study identified reversible oxidative modifications of the P-loop cysteine in FN3K and FN3KRP in both mouse and human tissues (48), suggesting that a regulatory mechanism of reversible P-loop oxidation is likely operative in cells and evolutionarily conserved.

The identification of redox-active cysteines in FN3Ks also opens up the possibility of a feedback regulation mechanism in which FN3K activity is controlled by its catalytic by-product, 3-deoxyglucosone, which is known to contribute to oxidative stress (21). We speculate that the accumulation of advanced glycation end products such as 3-deoxyglucosone drives the conformational ensemble of FN3K species toward an inactive dimeric form through the oxidation of the P-loop cysteine, whereas reduced levels maintain FN3K in an active reduced form (Fig. 9). Such a feedback inhibition mechanism might explain how the essential deglycation functions of FN3K are carried out in cells without contributing to oxidative stress. Consistent with this view, our biochemical and mutational studies confirmed that inhibited dimeric species predominate in the absence of reducing agents, whereas active dimeric or monomeric species may dominate in the presence of reducing agents. Moreover, our comparative metabolomics study of the HsFN3K WT and KO in HepG2 liver cells revealed alteration in redox-sensitive metabolites, namely, gluta-

thione. Increased cellular glutathione in the KO relative to WT suggests potential links between FN3K functions and oxidative stress response that needs to be tested in future studies. In particular, delineating the pathways that link the redox-active metabolites identified in our study with HsFN3K-mediated deglycation functions reported recently in oncogenesis (20) will be a major goal moving forward.

Redox control of FN3K may also explain the altered glycation patterns observed in plant and human proteomes (49–52) and facilitate deglycation functions to be carried out in different cellular compartments. Our studies on AtFN3K (without the signal peptide) revealed nuclear and mitochondrial localization (fig. S8). HsFN3K is localized in the mitochondria (53) and has been detected in red blood cells and serum samples. Mitochondria generate reactive oxygen species, which can mediate redox signaling through oxidation of SH groups in cysteine residues in proteins (54–56). The presence of a redox-sensitive P-loop cysteine (Cys²⁴) in HsFN3K further suggests that redox regulation of FN3K is physiologically relevant.

The P-loop Cys is conserved among FN3K orthologs from diverse prokaryotic and eukaryotic organisms, and our studies indicate that the HsFN3K is also redox sensitive. In contrast to the activation loop, which appears to have evolved as a flexible motif for ePK regulation by phosphorylation, the P-loop is fundamentally conserved in diverse ATP-fold enzymes, where it plays a critical role in clamping ATP and positioning it for efficient catalysis. Here, we show that conformational control of the P-loop by reactive cysteines is an ancient mode of regulation. Several eukaryotic tyrosine kinases such as SRC, fibroblast growth factor receptor (FGFR), YES1, and FYN conserve cysteine residues at the Cys³² of AtFN3K equivalent position in the P-loop (fig. S9), suggesting potential redox regulation of these kinases as well. Both SRC and FGFR have previously been shown to be redox-regulated through Cys oxidation mechanisms in the P-loop (57, 58). However, whether these kinases also form a strand-exchange dimer such as AtFN3K is not known, and it will be interesting to attempt to solve the structure of Tyr kinases crystallized under different oxidizing conditions.

Last, HsFN3K and HsFN3KRP are implicated in diseases such as diabetic neuropathy and retinopathy, and more recently, in cancer (20). However, developing therapeutic strategies for FN3Ks is potentially a double-edged sword because inhibition of FN3K activity can result in the accumulation of glycated proteins, whereas activation of FN3Ks might result in the accumulation of 3-deoxyglucosone, a potent generator of oxidative stress. On the basis of our findings, we propose a combinatorial drug development approach, in which the active monomeric species and the reduced dimeric species are targeted through the development of thiol-interacting agents. These might

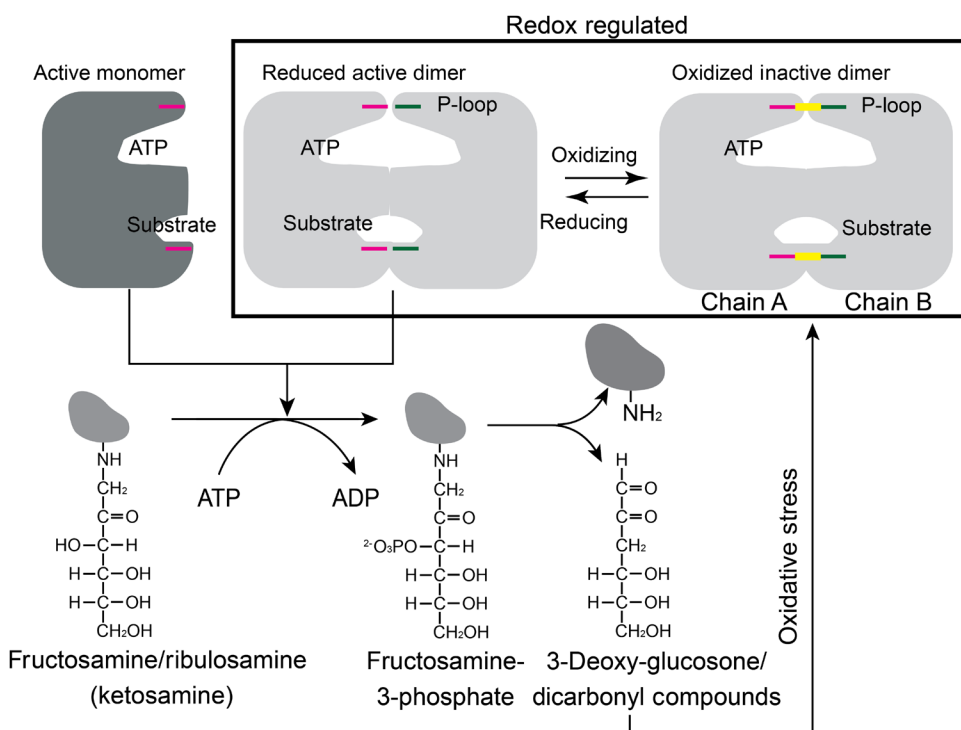


Fig. 9. Proposed redox feedback regulation of plant and mammalian FN3Ks. Cartoon showing the possible relationship between redox regulation of FN3K activity and its physiological function. The disulfide is colored in yellow.

be developed to help normalize cellular protein glycan homeostasis, depending on the indication and redox balance in the appropriate tissue and the availability of redox-active Cys residues in FN3K targets.

MATERIALS AND METHODS

Expression and purification of AtFN3K WT and Cys-to-Ala mutants

AtFN3K inserted into pET-15b expression vector was provided by E. Van Shaftingen (Université Catholique of Louvain, Brussels, Belgium). Site-directed mutagenesis was performed using the Q5 Hot Start High Fidelity Kit from New England Biolabs. Vectors were transformed into *E. coli* BL21(DE3) pLysS (Roche) cells, and coexpression with GroEL was performed at 16°C for 18 hours in 500 ml of Luria-Bertani medium containing ampicillin (100 µg/liter) and chloramphenicol (25 µg/liter). The bacterial extract was resuspended in 50 mM sodium phosphate buffer (pH 7.8), 300 mM NaCl, and 10% (v/v) glycerol (buffer A) with 1 mM phenylmethylsulfonyl fluoride and 3 mM 2-mercaptoethanol (βME). The solution was sonicated on ice, and the lysate was centrifuged at 15,000g for 45 min at 4°C. The supernatant was then passed through 0.5 ml of Talon resin previously equilibrated with buffer A without βME. The column was washed with 20 ml of buffer B [50 mM sodium phosphate buffer (pH 7.8), 1 M NaCl, and 10% (v/v) glycerol], followed by a wash with 100 ml of buffer B containing 10 mM imidazole. The protein was then eluted with buffer A without βME containing 250 mM imidazole. The purity of the protein was checked by SDS-PAGE, and the fractions with the protein were dialyzed against buffer A without glycerol and later against buffer C [25 mM Hepes (pH 7.8), 300 mM NaCl, and 10% (v/v) glycerol]. The protein was snap-frozen with liquid nitrogen and stored at –80°C. Recombinant His-HsFN3K was coexpressed with GroEL in *E. coli* as well.

Crystallization, phasing, and refinement

Recombinant AtFN3K WT was dialyzed into a buffer containing 50 mM NaCl and 15 mM Hepes at pH 8.0, concentrated to ~30 mg/ml, and quantified using the extinction coefficient (absorbance 0.1%: 1.576) calculated by ProtParam (59). The protein was crystallized at 20°C using hanging drop vapor diffusion with 2-µl drops (1:1 protein-to-reservoir ratio). Crystals grew from a reservoir of 2 M ammonium sulfate, 0.1 M MES (pH 5.5), 3.28 mM MgCl₂, and 1.9 mM AMP-PNP. Crystals were cryoprotected with the reservoir solution supplemented with 10% cryoprotectant (1:1:1 ratio of ethylene glycol, dimethyl sulfoxide, and glycerol) and flash cooled in liquid nitrogen. The diffraction data were collected at the SER-CAT 22-ID beamline at the Argonne National Laboratory using a Rayonix 300HS detector and processed using X-ray Detector Software (XDS) (60). Five percent of the data were set aside for cross-validation. The structure was solved by molecular replacement in Phenix (61) using a multiple model template [structures from *T. fusca* (PDB code 3F7W), *Histophilus somnus* (PDB code 3JR1), and *E. coli* (PDB code 5IGS) were used] with trimmed side chains and weighted according to structure and homology. Sequence matching and model building were performed using Phenix AutoBuild (61). Automated refinement in Phenix (61) and iterative manual fitting using Coot (62) produced the final model (table S1). The B-factors were refined using Translation/Libration/Screw (TLS) (63).

Distribution of χ^3 angle and C α -C α distance

We downloaded the dataset of culled crystal structures with unique disulfides from (64) and selected structures with a resolution of less than or equal to 1.5 Å to plot the histogram in Fig. 4B.

SDS-polyacrylamide gel electrophoresis

The enzyme (15 µg) was incubated with distilled H₂O or redox agents (DTT/H₂O₂) in a total volume of 15 µl. After 20 min, 5 µl of 4× sample buffer without βME was added, and the protein was denatured at 100°C for 5 min. The sample (10 µl) was loaded onto a 12% SDS-PAGE gel. The gels were stained with Coomassie for an hour and destained with water for several hours. Similarly, 3 to 5 µg of the enzyme (15-µl volume) was incubated with 20 mM NEM or buffer [15 mM Hepes (pH 7.8), 300 mM NaCl, and 10% (v/v) glycerol] for 5 min at room temperature before adding 4× sample buffer with (reducing) or without (nonreducing) 2.8 M βME.

Sequence alignment

Representative FN3K orthologs were downloaded from UniProt (65) and National Center for Biotechnology Information (66) and aligned using MUltiple Sequence Comparison by Log-Expectation (MUSCLE) (67). ePKs with P-loop cysteine conserved were identified using previously curated alignment profiles that included ePKs and small-molecule kinase sequences, including FN3Ks (22, 23, 68, 69).

Expression analysis

Human tumor expression data were obtained from the National Cancer Institute's Genomic Data Commons Data Portal (downloaded 10 February 2017) (70). RNA sequencing data were available for 11,574 samples (10,833 tumor samples and 741 normal samples). Read count for each gene was normalized by the fragments per kilobase of transcript per million mapped reads upper quartile method (71). Z score for each gene was calculated on the basis of deviation from the normalized mean expression levels (in logarithmic scale) for each sample.

Size exclusion chromatography

About 4.5 mg of AtFN3K WT and triple cysteine mutants purified using coexpression with GroEL/ES chaperone (9 mg/ml in concentration) was passed through HiLoad 16/1600 Superdex 200-pg column at a flow rate of 1 ml/min with a fractionation volume of 1 ml. Hepes (25 mM) (pH 7.8), 300 mM NaCl, and 10% (v/v) glycerol were used as running buffer. SEC was performed at 4°C. For bovine serum albumin (BSA)-lysozyme standard, 250 µl of BSA (4 mg/ml) and lysozyme each in running buffer were mixed and loaded on the column. For AtFN3K WT and triple cysteine mutants purified without GroEL chaperone (fig. S3A), SEC was performed at a flow rate of 0.15 ml/min.

PK/LDH enzyme assays

A total of 1.0 µg (5 µl) of FN3K homologs (*A. thaliana*, *T. fusca*, and *L. plantarum*)/mutants/dimer and 10 µg (5 µl) of HsFN3K, 28 mM ribulose-N- α -Ac-lysine (10 µl) in the presence or absence of 20 mM DTT (5 µl; final concentration, 2 mM), were mixed with 20 µl of solution prepared by mixing the following: 150 µl of 5× kinase buffer [160 mM Hepes (pH 7.4), 80 mM MgCl₂, 1.2 M NaCl, and 40% (v/v) glycerol], 15 µl of 250 mM phosphoenolpyruvic acid, 45 µl of PK/LDH mix [PK (600 to 100 U/ml) and LDH (900 to 1400 U/ml)], and 90 µl of 37.5 mM nicotinamide adenine dinucleotide.

The reaction was started by adding 10 μ l of 5 mM ATP (final concentration, 1 mM). The final reaction volume was 50 μ l per well. The 96-well plate was immediately placed in a plate reader (Biotek Synergy H4), and the absorbance was measured at 340 nm at 35°C continuously for 2.5 hours. Proteins were stored in buffer D [25 mM Hepes (pH 7.4), 300 mM NaCl, and 10% (v/v) glycerol]. Buffer D was also used as mock buffer as needed.

NMR real-time assay

One hundred micrograms of protein was incubated with 2 mM ribuloselysine and 600 μ M ATP in 25 mM Hepes (pH 8.0) and 5 mM MgCl₂ prepared in D₂O. The reaction was monitored for 50 min by acquiring subsequent 1D 1H PURGE (Presaturation Utilizing Relaxation Gradients and Echoes) spectra. All spectra were acquired at 22°C on an 800-MHz AVANCE NEO (Bruker) NMR spectrometer equipped with a z-gradient triple resonance TCI cryoprobe and normalized and referenced using ¹H signals of 4,4-dimethyl-4-silapentane-1-sulfonic acid (DSS). Thirty-two scans were acquired during each experiment with an acquisition time of 1.25 s. The spectra were processed using NMRpipe and Matrix Laboratory (MATLAB).

Sedimentation velocity

The triple cysteine mutant (C32A/C236A/C196A) was dialyzed into 25 mM Hepes (pH 7.8), 300 mM NaCl, 2 mM MgCl₂, 100 μ M ATP, and 1 M glycerol, and the protein was quantified using an Agilent 8453 ultraviolet-visible with an ϵ 280 of 55,810 M⁻¹ cm⁻¹ determined by ProtParam (59). The sample was diluted to a final protein concentration of 10 μ M and then loaded into 12-mm double-sector Epon centerpieces equipped with quartz windows. The cell was loaded into An60 Ti rotor and equilibrated for 1 hour at 20°C. Sedimentation velocity data were collected using an Optima XLA analytical ultracentrifuge (Beckman Coulter) at a rotor speed of 50,000 rpm at 20°C. Data were recorded at 280 nm in radial step sizes of 0.003 cm. SEDNTERP (72) was used to model the partial specific volume of AtFN3K (0.713293 ml/g), as well as the density (1.0353 g/ml) and the viscosity (0.013277 P) of the buffer. SEDFIT (73) was used to analyze the raw sedimentation data. Data were modeled as continuous c(s) distribution and were fit using baseline, meniscus, frictional coefficient, and systematic time-invariant and radial-invariant noise. Fit data for the experiment had an RMSD in the range of 0.005 to 0.007 arbitrary units. Predicted sedimentation coefficient (s) values for AtFN3K monomer (2.2 S) and dimer (3.6 S) were calculated from the atomic coordinate of AtFN3K using HYDROPRO (74). Data fit and c(s) distribution plots were generated using GUSI (75).

Diamide treatment of HEK 293T cells

HEK 293T cells were cultured in Dulbecco's modified Eagle's medium containing 10% fetal bovine serum on a 6-cm plate (six plates in total) and allowed to grow overnight. Cells were transfected with 10 μ g of Flag-tagged HsFN3K (EX-W1392-M46, GeneCopoeia) using calcium phosphate transfection protocol (76). Cells were allowed to grow for 48 hours. After 48 hours, cells were treated with indicated concentrations of diamide (Sigma-Aldrich) for 2 hours. Cells were lysed in buffer containing 50 mM tris-HCl (pH 7.5), 150 mM NaCl, 10% glycerol, 1% Triton X-100, and 1 \times protease inhibitor cocktail (EMD Millipore). Total cell lysate was spun at 15,000 rpm for 10 min in a refrigerated centrifuge. Proteins were resolved on a 12%

SDS-PAGE gel, transferred on polyvinylidene difluoride membrane and detected by Western blotting using anti-Flag antibody (Cell Signaling Technology).

CRISPR KO cell line and metabolomics

HepG2 cells were transfected with FN3K Double Nickase Plasmid (sc-412985-NIC, Santa Cruz Biotechnology) and selected with puromycin according to the manufacturer's protocol. FN3K deletion was confirmed by Western blotting using an anti-FN3K antibody (Invitrogen) (fig. S7). Stable cell line stocks were made from single-cell colony. Cell cultures for both cell lines were grown simultaneously with identical medium components. Upon achieving ~80% confluence in 10-cm culture dish, culture medium was removed, and cell monolayer was washed with phosphate-buffered saline. Adherent cells were harvested in ice-cold 80% methanol extraction solvent and flash-frozen in liquid nitrogen. Aqueous metabolites were extracted by vortexing/lysing cell pellets in the extraction solvent and collecting the supernatant. About 10% of the supernatant was taken from each sample to form an internal pooled sample. The solvent was then evaporated to produce dried extracts using a CentriVap Benchtop Vacuum Concentrator (Labconco, Kansas City, MO, USA). Extracts were reconstituted in a deuterium oxide (Cambridge Isotope Laboratories) 100 mM phosphate buffer (pH 7.4) with 1/3 mM DSS (Cambridge Isotope Laboratories), which was referenced to 0.0 parts per million (ppm). ¹H NMR spectra were acquired on all samples using noesypr1d pulse sequence on an 800-MHz Bruker Avance III HD spectrometer equipped with a SampleJet sample changer (Bruker BioSpin). ¹H-¹³C heteronuclear single-quantum correlation and ¹H-¹H total correlation spectroscopy spectra were acquired on the internal pooled sample for metabolite annotation. Two-dimensional spectra were processed with NMRpipe (77) and uploaded to the Complex Mixture Analysis by NMR webserver (COLMARm) (78). Metabolite annotations were assigned a confidence score from 1 to 5 as previously described (table S2) (79). ¹H NMR spectra were phased, and baseline was corrected using TopSpin software (Bruker BioSpin) and then further processed and analyzed with an in-house MATLAB toolbox (80). After referencing to DSS, end removal, solvent region removal, and alignment using the peak alignment by fast Fourier transform algorithm (81), spectra were normalized using the probabilistic quotient normalization algorithm (82). Spectral features that were not substantially overlapped and assigned to annotated metabolites were integrated to get the relative quantification of metabolites for all samples. Annotated metabolites were then tested for statistical significance between cell lines via two-tailed *t* test, and *P* values were corrected for false discovery rate using the Benjamini-Hochberg method (table S2) (83). All spectral data, sample preparation, and processing details will be made available on the Metabolomics Workbench (<https://metabolomicsworkbench.org>).

Construction of plasmids for transient transformations of *Nicotiana benthamiana*

For constructs used in the transient assays, full-length WT or mutant coding sequences (CDS) of AtFN3K were cloned into pENTR/D-TOPO gateway entry vector (Invitrogen) following the manufacturer's protocol. The coding regions were recombined into binary destination expression vector: pSITE-2CA N-terminal green fluorescent protein (GFP) fusion.

Agrobacterium tumefaciens strain C58C1 was used for the transient transformation. Colonies carrying the binary plasmids were

grown at 28°C on plates with lysogeny broth (LB) medium that contained gentamycin (50 µg/ml) and rifampicin (25 µg/ml) for selection of the strain and spectinomycin (100 µg/ml) for selection of the binary vector. For agroinfiltration, single colonies were grown overnight in 3-ml LB (28°C, 220 rpm). Fifty microliters of the agro suspension was added to 5-ml LB, and the culture was grown overnight. The agro was pelleted by centrifuging at 4000 rpm for 20 min or 50,000 rpm for 15 min, and the suspension was adjusted to an optical density at 600 nm of 0.2 to 0.3 in infiltration buffer containing 10 mM MgCl₂, 10 mM MES (pH 5.7), and 150 mM acetosyringone (pH 5.6) and incubated at room temperature for 3 hours before infiltration. To enhance transient expression of the fusion proteins, the viral suppressor of gene silencing p19 protein was coexpressed. For coinfiltration, equal volumes of cultures were mixed and infiltrated into *N. benthamiana* leaves through the abaxial surface using a 1-ml needleless syringe (Becton, Dickinson, and Company). Plants were then kept in a growth room at 24°/22°C with a 16:8-hour light/dark photoperiod for 48 to 72 hours.

Subcellular localization epifluorescence and confocal microscopy

N. benthamiana leaf samples 70 to 90 hours after infiltration (about 0.25 cm² from the infiltrated area) were mounted in water and viewed directly with a Zeiss LSM 880 confocal scanning microscope using an oil immersion objective 40× Plan-Apochromat 1.4 NA (numerical aperture of 1.4). Fluorescence was excited using 488-nm light for GFP. GFP emission fluorescence was selectively detected at 490 to 540 nm using the Zen 2.3 SP1 software. Each experiment was repeated three times.

Synthesis of ribulose-*N*- α -Ac-lysine

A solution of *N*- α -acetyl-L-lysine (0.5 g, 2.66 mmol) and D-ribose (1.6 g, 10.64 mmol) in methanol (100 ml) was stirred at 50°C for 4 hours under argon gas. The solvent was evaporated under vacuum, and the residue obtained was purified over silica gel column by flash chromatography (*R*_f = 0.14; EtOAc/MeOH/H₂O, 5/3/2, v/v/v). The product obtained was further purified over a column of Dowex 50 x 8 H⁺ resin (0.6 cm by 5 cm) cation exchange resin using 150 mM NaCl as an eluent and desalted over a P-2 column using H₂O as an eluent. The desired fractions were combined, concentrated, and lyophilized to afford the product as white solid (0.55 g, 64.7%); low-resolution mass spectrometry (LRMS) [electrospray ionization (ESI): calculated for C₁₃H₂₅N₂O₇ [M + H]⁺, 321.16; found, 321.09. Synthesized ribulose-*N*- α -Ac-lysine was characterized using NMR and ESI (fig. S11) and used as substrate in the PK/LDH assays.

Statistical analysis

$\Delta G P$ value reported for solvation free energy was calculated by the PISA server (33). Briefly, it estimates the statistical significance of observing lower than observed ΔG values when the interface atoms are picked randomly from the protein surface with the equivalent interface area. $\Delta G P$ values of <0.5 are statistically significant (84). Statistical significance of metabolite differences between WT and KO (table S2) was determined using two-tailed *t* test. *P* values were then corrected for false discovery rate using the Benjamini-Hochberg method.

SUPPLEMENTARY MATERIALS

stke.sciencemag.org/cgi/content/full/13/639/eaax6313/DC1

Fig. S1. Hydrogen bonds and disulfide bridges between chain A and chain B in WT AtFN3K.

Fig. S2. Oxidized monomeric species are an artifact of the SDS-PAGE gel.

Fig. S3. WT and triple cysteine mutant (C32A/C236A/C196A) AtFN3K exist as two distinct species.

Fig. S4. Reducing and nonreducing SDS-PAGE of dimer and monomer fractions of WT and triple cysteine mutant AtFN3K.

Fig. S5. Effects of thiol reagents on the activity of WT and cysteine mutant AtFN3K.

Fig. S6. P-loop cysteine (Cys²⁴) is critical for the formation of disulfide-linked dimer in HsFN3K.

Fig. S7. Western blot of HsFN3K KO in HepG2 cells.

Fig. S8. WT and C32A/C236A AtFN3K localize to the nucleus.

Fig. S9. Multiple sequence alignment showing the conservation of P-loop cysteine in selected human ePKs and FN3Ks.

Fig. S10. FN3K and FN3KRP expression levels in human tumors.

Fig. S11. Spectral data of ribulose-*N*- α -Ac-lysine.

Table S1. Data collection and refinement statistics of WT AtFN3K.

Table S2. Metabolites identified in extracts of WT HepG2 and FN3K-KO cells.

References (88, 89)

[View/request a protocol for this paper from Bio-protocol.](#)

REFERENCES AND NOTES

1. L. C. Maillard, The action of amino acids on sugar; the formation of melanoidin by a methodic route. *Comptes Rendus Hebd. Seances Acad. Sci.* **154**, 66–68 (1912).
2. M. Teodorowicz, J. van Neerven, H. Savelkoul, Food processing: The influence of the maillard reaction on immunogenicity and allergenicity of food proteins. *Nutrients* **9**, 835 (2017).
3. J. E. Hodge, The Amadori rearrangement. *Adv. Carbohydr. Chem.* **10**, 169–205 (1955).
4. H. F. Bunn, P. J. Higgins, Reaction of monosaccharides with proteins: Possible evolutionary significance. *Science* **213**, 222–224 (1981).
5. J. W. Baynes, N. G. Watkins, C. I. Fisher, C. J. Hull, J. S. Patrick, M. U. Ahmed, J. A. Dunn, S. R. Thorpe, The Amadori product on protein: Structure and reactions. *Prog. Clin. Biol. Res.* **304**, 43–67 (1989).
6. E. Van Schaftingen, F. Collard, E. Wiame, M. Veiga-da-Cunha, Enzymatic repair of Amadori products. *Amino Acids* **42**, 1143–1150 (2012).
7. J. B. Veronika, M. Deppe, T. O'Connell, K.-H. Maurer, F. Meinhardt, Enzymatic deglycation of Amadori products in bacteria: Mechanisms, occurrence and physiology functions. *Appl. Microbiol. Biotechnol.* **90**, 399–406 (2011).
8. P. Gkogkolou, M. Böhm, Advanced glycation end products. Key players in skin aging? *Dermatoendocrinol* **4**, 259–270 (2012).
9. G. D. François Collard, V. Stroobant, G. Matthijs, E. Van Schaftingen, A mammalian protein homologous to fructosamine-3-kinase acting on psicossamines and ribulosamines but not on fructosamines. *Diabetes* **52**, 2888–2895 (2003).
10. M. H. R. Ghislain Delpierre, F. Collard, V. Stroobant, F. Vanstapel, H. Santos, E. Van Schaftingen, Identification, cloning, and heterologous expression of a mammalian fructosamine-3-kinase. *Diabetes* **49**, 1627–1634 (2000).
11. S. H. Benjamin, S. Szewerglod, P. J. Beisswenger, Human fructosamine-3-kinase. Purification, sequencing, substrate specificity, and evidence of activity in vivo. *Diabetes* **50**, 2139–2147 (2001).
12. R. G. Juliette Fortpied, V. Stroobant, E. van Schaftingen, Plant ribulosamine/erythrosamine 3-kinase, a putative protein-repair enzyme. *Biochem. J.* **388**, 795–802 (2005).
13. P. J. B. James, R. Conner, B. S. Szewergold, The expression of the genes for fructosamine-3-kinase and fructosamine-3-kinase-related protein appears to be constitutive and unaffected by environmental signal. *Biochem. Biophys. Res. Commun.* **323**, 932–936 (2004).
14. G. D. Jérôme Delplanque, F. R. Opperdoes, E. Van Schaftingen, Tissue distribution and evolution of fructosamine 3-kinase and fructosamine 3-kinase-related protein. *J. Biol. Chem.* **279**, 46606–46613 (2004).
15. J. F. Rita Gemayel, R. Rzem, D. Vertommen, M. Veiga-da-Cunha, E. Van Schaftingen, Many fructosamine 3-kinase homologues in bacteria are ribulosamine/erythrosamine 3-kinase potentially involved in protein deglycation. *FEBS J.* **274**, 4360–4374 (2007).
16. T. R. Brown, B. Su, K. A. Brown, M. A. Schwartz, A. M. Tobia, F. Kappler, Modulation of in vivo 3-deoxyglucosone levels. *Biochem. Soc. Trans.* **31**, 1433–1437 (2003).
17. S. M. Pascal, M. Veiga-da-Cunha, P. Gilon, E. Van Schaftingen, J. C. Jonas, Effects of fructosamine-3-kinase deficiency on function and survival of mouse pancreatic islets prolonged culture in high glucose or ribose concentrations. *Am. J. Physiol. Endocrinol. Metab.* **298**, E586–E596 (2010).
18. H. Kusunoki, S. Miyata, T. Ohara, B.-F. Liu, A. Uriuhara, H. Kojima, K. Suzuki, H. Miyazaki, Y. Yamashita, K. Inaba, M. Kasuga, Relation between serum 3-deoxyglucosone and development of diabetic microangiopathy. *Diabetes Care* **26**, 1889 (2003).
19. T. Niwa, N. Takeda, H. Yoshizumi, A. Tatematsu, M. Ohara, S. Tomiyama, K. Niimura, Presence of 3-deoxyglucosone, a potent protein crosslinking intermediate of Maillard reaction, in diabetic serum. *Biochem. Biophys. Res. Commun.* **196**, 837–843 (1993).
20. V. R. Sanghvi, J. Leibold, M. Mina, P. Mohan, M. Berishaj, Z. Li, M. M. Miele, N. Lailier, C. Zhao, E. de Stanchina, A. Viale, L. Akkari, S. W. Lowe, G. Ciriello, R. C. Hendrickson, H.-G. Wendel, The oncogenic action of NRF2 depends on de-glycation by fructosamine-3-kinase. *Cell* **178**, 807–819.e21 (2019).

21. T. Niwa, S. Tsukushi, 3-deoxyglucosone and AGEs in uremic complications: Inactivation of glutathione peroxidase by 3-deoxyglucosone. *Kidney Int. Suppl.* **78**, S37–S41 (2001).
22. N. Kannan, S. S. Taylor, Y. Zhai, J. C. Venter, G. Manning, Structural and functional diversity of the microbial kinome. *PLOS Biol.* **5**, e17 (2007).
23. K. Oruganty, E. E. Talevich, A. F. Neuwald, N. Kannan, Identification and classification of small molecule kinases: Insights into substrate recognition and specificity. *BMC Evol. Biol.* **16**, 7 (2016).
24. V. S. Tagliabracchi, S. E. Wiley, X. Guo, L. N. Kinch, E. Durrant, J. Wen, J. Xiao, J. Cui, K. B. Nguyen, J. L. Engel, J. J. Coon, N. Grishin, L. A. Pinna, D. J. Pagliarini, J. E. Dixon, A single kinase generates the majority of the secreted phosphoproteome. *Cell* **161**, 1619–1632 (2015).
25. A. Sreelatha, S. S. Yee, V. A. Lopez, B. C. Park, L. N. Kinch, S. Pilch, K. A. Servage, J. Zhang, J. Jiou, M. Karasiewicz-Urbańska, M. Lobočka, N. V. Grishin, K. Orth, R. Kucharczyk, K. Pawłowski, D. R. Tomchick, V. S. Tagliabracchi, Protein AMPylation by an evolutionarily conserved pseudokinase. *Cell* **175**, 809–821.e19 (2018).
26. A. Kwon, S. Scott, R. Taujale, W. Yeung, K. J. Kochut, P. A. Eyers, N. Kannan, Tracing the origin and evolution of pseudokinases across the tree of life. *Sci. Signal.* **12**, eaav3810 (2019).
27. N. Kannan, A. F. Neuwald, Did protein kinase regulatory mechanisms evolve through elaboration of a simple structural component? *J. Mol. Biol.* **351**, 956–972 (2005).
28. B. Nolen, S. Taylor, G. Ghosh, Regulation of protein kinases: Controlling activity through activation segment conformation. *Mol. Cell* **15**, 661–675 (2004).
29. D. P. Byrne, S. Shrestha, M. Galler, M. Cao, L. A. Daly, A. E. Campbell, C. E. Eyers, E. A. Veal, N. Kannan, P. A. Eyers, Aurora A regulation by reversible cysteine oxidation reveals evolutionary-conserved redox control of Ser/Thr protein kinase activity. *Sci. Signal.* **13**, eaax2713 (2020).
30. A. C. Bastidas, M. S. Deal, J. M. Steichen, Y. Guo, J. Wu, S. S. Taylor, Phosphoryl transfer by protein kinase A is captured in a crystal lattice. *J. Am. Chem. Soc.* **135**, 4788–4798 (2013).
31. L. Holm, P. Rosenström, Dali server: Conservation mapping in 3D. *Nucleic Acids Res.* **38**, W545–W549 (2010).
32. D. H. Fong, D. L. Burk, J. Blanchet, A. Y. Yan, A. M. Berghuis, Structural basis for kinase-mediated macrolide antibiotic resistance. *Structure* **25**, 750–761.e5 (2017).
33. E. Krissinel, K. Henrick, Inference of macromolecular assemblies from crystalline state. *J. Mol. Biol.* **372**, 774–797 (2007).
34. B. Schmidt, L. Ho, P. J. Hogg, Allosteric disulfide bonds. *Biochemistry* **45**, 7429–7433 (2006).
35. N. Haworth, L. L. Feng, M. Wouters, High torsional energy disulfides: Relationship between cross-strand disulfides and right-handed staples. *J. Bioinform Comput Biol.* **4**, 155–168 (2006).
36. M. A. Wouters, S. W. Fan, N. L. Haworth, Disulfides as redox switches: From molecular mechanisms to functional significance. *Antioxid. Redox Signal.* **12**, 53–91 (2009).
37. N. Srinivasan, R. Sowdhamini, C. Ramakrishnan, P. Balam, Conformations of disulfide bridges in proteins. *Int. J. Pept. Protein Res.* **36**, 147–155 (1990).
38. G. T. Hanson, R. Aggeler, D. Oglesbee, M. Cannon, R. A. Capaldi, R. Y. Tsien, S. J. Remington, Investigating mitochondrial redox potential with redox-sensitive green fluorescent protein indicators. *J. Biol. Chem.* **279**, 13044–13053 (2004).
39. J. D. Gregory, The stability of N-ethylmaleimide and its reaction with sulphydryl groups. *J. Am. Chem. Soc.* **77**, 3922–3923 (1955).
40. N. S. Kosower, E. M. Kosower, in *Biothiols Part A Monothioles and Dithiols, Protein Thiols, and Thiol Radicals* (Academic Press, 1995), vol. 251, pp. 123–133.
41. N. S. Kosower, E. M. Kosower, in *Methods in Enzymology* (Academic Press, 1987), vol. 143, pp. 264–270.
42. G. Ferrer-Sueta, B. Manta, H. Botti, R. Radi, M. Trujillo, A. Denicola, Factors affecting protein thiol reactivity and specificity in peroxide reduction. *Chem. Res. Toxicol.* **24**, 434–450 (2011).
43. I. Gout, Coenzyme A, protein CoAlation and redox regulation in mammalian cells. *Biochem. Soc. Trans.* **46**, 721–728 (2018).
44. I. Amelio, F. Cutruzzola, A. Antonov, M. Agostini, G. Melino, Serine and glycine metabolism in cancer. *Trends Biochem. Sci.* **39**, 191–198 (2014).
45. J. Garcia-Bermudez, L. Baudrier, K. La, X. G. Zhu, J. Fidelin, V. O. Sviderskiy, T. Papagiannakopoulos, H. Molina, M. Snuderl, C. A. Lewis, R. L. Possemato, K. Birsoy, Aspartate is a limiting metabolite for cancer cell proliferation under hypoxia and in tumours. *Nat. Cell Biol.* **20**, 775–781 (2018).
46. C. H. Fiske, Y. Subbarow, The nature of the “inorganic phosphate” in voluntary muscle. *Science* **65**, 401–403 (1927).
47. S. Akter, L. Fu, Y. Jung, M. L. Conte, J. R. Lawson, W. T. Lowther, R. Sun, K. Liu, J. Yang, K. S. Carroll, Chemical proteomics reveals new targets of cysteine sulfenic acid reductase. *Nat. Chem. Biol.* **14**, 995–1004 (2018).
48. H. Xiao, M. P. Jedrychowski, D. K. Schweppe, E. L. Huttlin, Q. Yu, D. E. Heppner, J. Li, J. Long, E. L. Mills, J. Szpyt, Z. He, G. Du, R. Garrity, A. Reddy, L. P. Vaites, J. A. Paulo, T. Zhang, N. S. Gray, S. P. Gygi, E. T. Chouchani, A quantitative tissue-specific landscape of protein redox regulation during aging. *Cell* **180**, 968–983.e24 (2020).
49. T. Bilova, E. Lukasheva, D. Brauch, U. Greifenhagen, G. Paudel, E. Tarakhovskaya, N. Frolova, J. Mittasch, G. U. Balcke, A. Tissier, N. Osmolovskaya, T. Vogt, L. A. Wessjohann, C. Birkemeyer, C. Milkowski, A. Frolov, A snapshot of the plant glycosylated proteome: Structural, functional, and mechanistic aspects. *J. Biol. Chem.* **291**, 7621–7636 (2016).
50. U. Greifenhagen, V. D. Nguyen, J. Moschner, A. Giannis, A. Frolov, R. Hoffmann, Sensitive and site-specific identification of carboxymethylated and carboxyethylated peptides in tryptic digests of proteins and human plasma. *J. Proteome Res.* **14**, 768–777 (2015).
51. R. Schmidt, D. Böhme, D. Singer, A. Frolov, Specific tandem mass spectrometric detection of AGE-modified arginine residues in peptides. *J. Mass Spectrom.* **50**, 613–624 (2015).
52. Q. Zhang, N. Tang, A. A. Schepmoes, L. S. Phillips, R. D. Smith, T. O. Metz, Proteomic profiling of nonenzymatically glycosylated proteins in human plasma and erythrocyte membranes. *J. Proteome Res.* **7**, 2025–2032 (2008).
53. P. J. Thul, L. Åkesson, M. Wiking, D. Mahdessian, A. Geladaki, H. A. Blal, T. Alm, A. Asplund, L. Björk, L. M. Breckels, A. Bjelkström, F. Danielsson, L. Fagerberg, J. Fall, L. Gatto, C. Gnann, S. Hober, M. Hjelmare, F. Johansson, S. Lee, C. Lindskog, J. Mulder, C. M. Mulvey, P. Nilsson, P. Oksvold, J. Rockberg, R. Schutten, J. M. Schwenk, Å. Sivertsson, E. Sjöstedt, M. Skogs, C. Stadler, D. P. Sullivan, H. Tegel, C. Winsnes, C. Zhang, M. Zvalnen, A. Mardinoglu, F. Pontén, K. von Feilitzen, K. S. Lilley, M. Uhlén, E. Lundberg, A subcellular map of the human proteome. *Science* **356**, eaal3321 (2017).
54. D. E. Handy, J. Loscalzo, Redox regulation of mitochondrial function. *Antioxid. Redox Signal.* **16**, 1323–1367 (2012).
55. R. J. Mailloux, X. Jin, W. G. Willmore, Redox regulation of mitochondrial function with emphasis on cysteine oxidation reactions. *Redox Biol.* **2**, 123–139 (2014).
56. Y.-M. Go, D. P. Jones, Redox compartmentalization in eukaryotic cells. *Biochim. Biophys. Acta* **1780**, 1273–1290 (2008).
57. D. J. Kemble, G. Sun, Direct and specific inactivation of protein tyrosine kinases in the Src and FGFR families by reversible cysteine oxidation. *Proc. Natl. Acad. Sci. U.S.A.* **106**, 5070–5075 (2009).
58. D. E. Heppner, C. M. Dustin, C. Liao, M. Hristova, C. Veith, A. C. Little, B. A. Ahlers, S. L. White, B. Deng, Y.-W. Lam, J. Li, A. van der Vliet, Direct cysteine sulfenylation drives activation of the Src kinase. *Nat. Commun.* **9**, 4522 (2018).
59. E. Gasteiger, C. Hoogland, A. Gattiker, S. E. Duvaud, M. R. Wilkins, R. D. Appel, A. Bairoch, in *The Proteomics Protocols Handbook*, J. M. Walker, Ed. (Humana Press, 2005), pp. 571–607.
60. W. Kabsch, XDS. *Acta Crystallogr. D* **66**, 125–132 (2010).
61. P. D. Adams, P. V. Afonine, G. Bunkoczi, V. B. Chen, I. W. Davis, N. Echols, J. J. Headd, L.-W. Hung, G. J. Kapral, R. W. Grosse-Kunstleve, A. J. McCoy, N. W. Moriarty, R. Oeffner, R. J. Read, D. C. Richardson, J. S. Richardson, T. C. Terwilliger, P. H. Zwart, PHENIX: A comprehensive Python-based system for macromolecular structure solution. *Acta Crystallogr. D. Biol. Crystallogr.* **66**, 213–221 (2010).
62. P. Emsley, B. Lohkamp, W. G. Scott, K. Cowtan, Features and development of Coot. *Acta Crystallogr. D. Biol. Crystallogr.* **66**, 486–501 (2010).
63. A. Urzhumtsev, P. V. Afonine, P. D. Adams, TLS from fundamentals to practice. *Crystallogr. Rev.* **19**, 230–270 (2013).
64. E. Pijning Aster, J. Chiu, X. Yeo Reichelle, W. H. Wong Jason, J. Hogg Philip, Identification of allosteric disulfides from labile bonds in x-ray structures. *R. Soc. Open Sci.* **5**, 171058 (2018).
65. The UniProt Consortium, UniProt: The universal protein knowledgebase. *Nucleic Acids Res.* **46**, 2699–2699 (2018).
66. N. A. O’Leary, M. W. Wright, J. R. Brister, S. Ciufu, D. Haddad, R. McVeigh, B. Rajput, B. Robbette, B. Smith-White, D. Ako-Adjei, A. Astashyn, A. Badreddin, Y. Bao, O. Blinkova, V. Brover, V. Chetvermin, J. Choi, E. Cox, O. Ermolaeva, C. M. Farrell, T. Goldfarb, T. Gupta, D. Haft, E. Hatcher, W. Hlavina, V. S. Joardar, V. K. Kodali, W. Li, D. Maglott, P. Masterson, K. M. McGarvey, M. R. Murphy, K. O’Neill, S. Pujar, S. H. Rangwala, D. Rausch, L. D. Riddick, C. Schoch, A. Shkeda, S. S. Storz, H. Sun, F. Thibaud-Nissen, I. Tolstoy, R. E. Tully, A. R. Vatsan, C. Wallin, D. Webb, W. Wu, M. J. Landrum, A. Kimchi, T. Tatusova, M. DiCuccio, P. Kitts, T. D. Murphy, K. D. Pruitt, Reference sequence (RefSeq) database at NCBI: Current status, taxonomic expansion, and functional annotation. *Nucleic Acids Res.* **44**, D733–D745 (2016).
67. R. C. Edgar, MUSCLE: Multiple sequence alignment with high accuracy and high throughput. *Nucleic Acids Res.* **32**, 1792–1797 (2004).
68. D. I. McSkimming, S. Dastgheib, T. R. Baffi, D. P. Byrne, S. Ferries, S. T. Scott, A. C. Newton, C. E. Eyers, K. J. Kochut, P. A. Eyers, N. Kannan, KinView: A visual comparative sequence analysis tool for integrated kinome research. *Mol. Biosyst.* **12**, 3651–3665 (2016).
69. R. D. Finn, J. Mistry, J. Tate, P. Coghill, A. Heger, J. E. Pollington, O. L. Gavin, P. Gunasekaran, G. Ceric, K. Forslund, L. Holm, E. L. Sonnhammer, S. R. Eddy, A. Bateman, The Pfam protein families database. *Nucleic Acids Res.* **38**, D211–D222 (2010).
70. R. L. Grossman, A. P. Heath, V. Ferretti, H. E. Varmus, D. R. Lowy, W. A. Kibbe, L. M. Staudt, Toward a shared vision for cancer genomic data. *N. Engl. J. Med.* **375**, 1109–1112 (2016).
71. S. Anders, P. T. Pyl, W. Huber, HTSeq—A python framework to work with high-throughput sequencing data. *Bioinformatics* **31**, 166–169 (2015).

72. T. M. Laue, B. D. Shah, T. M. Ridgeway, S. L. Peletier, Computer-aided interpretation of analytical sedimentation data for proteins, in *Analytical Ultracentrifugation in Biochemistry and Polymer Science*, S. Harding, A. Rowe, J. Horton, Eds. (Royal Society of Chemistry, 1992), pp. 90–125.
73. P. Schuck, On the analysis of protein self-association by sedimentation velocity analytical ultracentrifugation. *Anal. Biochem.* **320**, 104–124 (2003).
74. A. Ortega, D. Amorós, J. García de la Torre, Prediction of hydrodynamic and other solution properties of rigid proteins from atomic- and residue-level models. *Biophys. J.* **101**, 892–898 (2011).
75. C. A. Brautigam, Calculations and publication-quality illustrations for analytical ultracentrifugation data. *Methods Enzymol.* **562**, 109–133 (2015).
76. R. E. Kingston, C. A. Chen, H. Okayama, Calcium Phosphate Transfection. *Current Protocols in Immunology* **31**, 10.13.11–10.13.19 (1999).
77. F. Delaglio, S. Grzesiek, G. Vuister, G. Zhu, J. Pfeifer, A. Bax, NMRPipe: A multidimensional spectral processing system based on UNIX pipes. *J. Biomol. NMR* **6**, 277–293 (1995).
78. K. Bingol, D.-W. Li, B. Zhang, R. Brüschweiler, Comprehensive metabolite identification strategy using multiple two-dimensional NMR spectra of a complex mixture implemented in the COLMARm web server. *Anal. Chem.* **88**, 12411–12418 (2016).
79. J. M. Walejko, A. Chelliah, M. Keller-Wood, A. Gregg, A. S. Edison, Global metabolomics of the placenta reveals distinct metabolic profiles between maternal and fetal placental tissues following delivery in non-labored women. *Metabolites* **8**, (2018).
80. S. L. Robinette, R. Ajredini, H. Rasheed, A. Zeinomar, F. C. Schroeder, A. T. Dossey, A. S. Edison, Hierarchical alignment and full resolution pattern recognition of 2D NMR spectra: Application to nematode chemical ecology. *Anal. Chem.* **83**, 1649–1657 (2011).
81. J. W. H. Wong, C. Durante, H. M. Cartwright, Application of fast fourier transform cross-correlation for the alignment of large chromatographic and spectral datasets. *Anal. Chem.* **77**, 5655–5661 (2005).
82. F. Dieterle, A. Ross, G. Schlotterbeck, H. Senn, Probabilistic quotient normalization as robust method to account for dilution of complex biological mixtures. Application in ¹H NMR metabolomics. *Anal. Chem.* **78**, 4281–4290 (2006).
83. Y. Benjamini, Y. Hochberg, Controlling the false discovery rate: A practical and powerful approach to multiple testing. *J. R. Stat. Soc. B. Methodol.* **57**, 289–300 (1995).
84. E. Krissinel, Crystal contacts as nature's docking solutions. *J. Comput. Chem.* **31**, 133–143 (2010).
85. D. H. Fong, A. M. Berghuis, Substrate promiscuity of an aminoglycoside antibiotic resistance enzyme via target mimicry. *EMBO J.* **21**, 2323–2331 (2002).
86. J. Zheng, E. A. Trafny, D. R. Knighton, N. Xuong, S. S. Taylor, L. F. Ten Eyck, J. M. Sowadski, 2.2 Å refined crystal structure of the catalytic subunit of cAMP-dependent protein kinase complexed with MnATP and a peptide inhibitor. *Acta Crystallogr. D Biol. Crystallogr.* **49**, 362–365 (1993).
87. Schrodinger, LLC, *The PyMOL Molecular Graphics System, Version 2.3.2.* (2019).
88. K. Diederichs, P. A. Karplus, Improved R-factors for diffraction data analysis in macromolecular crystallography. *Nat. Struct. Biol.* **4**, 269–275 (1997).
89. P. A. Karplus, K. Diederichs, Linking crystallographic model and data quality. *Science* **336**, 1030–1033 (2012).

Acknowledgments: We thank the staff at the Southeast Regional Collaborative Access Team (SER-CAT) at the Advanced Photon Source. We also thank E. Van Shaftingen (Université Catholique de Louvain, Brussels, Belgium) for the AtFN3K WT pET-15b construct. **Funding:** This work was initially supported by NSF funds to Kannan lab (MCB-1149106) and more recently by the NIH (R01GM114409) Pump-priming grant from the University of Georgia and University of Liverpool. Additional support for D.P.B. and P.A.E. was received from a Royal Society Research Grant and North West Cancer Research (CR1208). **Author contributions:** N. Kannan conceived and designed the project. S.S. and S.K. performed the experiments. C.E.S.-R. contributed to the mutational analysis. D.P.B. and P.A.E. contributed reagents and analyzed the redox data. N.R.K., R.K., and Z.A.W. contributed to the x-ray crystallography and structural analysis. H.W.K. collected and analyzed the sedimentation velocity data. C.P. and A.S.E. contributed to the NMR studies. M.C. and A.S.E. contributed to the metabolomic studies. N. Keyhaninejad and E.v.d.K. contributed to the localization studies on AtFN3K. P.C. and G.J.B. contributed to the synthesis and purification of ribuloselysine. N. Kannan and S.S. wrote the manuscript with contributions from all authors. **Competing interests:** The authors declare that they have no competing interests. **Data and materials availability:** Structural coordinate and structure factors are made available in the PDB (code 6OID). All other data needed to evaluate the conclusions in the paper are present in the paper or the Supplementary Materials.

Submitted 10 April 2019
Resubmitted 30 January 2020
Accepted 7 May 2020
Published 7 July 2020
10.1126/scisignal.aax6313

Citation: S. Shrestha, S. Katiyar, C. E. Sanz-Rodriguez, N. R. Kempainen, H. W. Kim, R. Kadirvelraj, C. Panagos, N. Keyhaninejad, M. Colonna, P. Chopra, D. P. Byrne, G. J. Boons, E. van der Knaap, P. A. E. Evers, A. S. Edison, Z. A. Wood, N. Kannan, A redox-active switch in fructosamine-3-kinases expands the regulatory repertoire of the protein kinase superfamily. *Sci. Signal.* **13**, eaax6313 (2020).

A redox-active switch in fructosamine-3-kinases expands the regulatory repertoire of the protein kinase superfamily

Safal Shrestha, Samiksha Katiyar, Carlos E. Sanz-Rodriguez, Nolan R. Kemppinen, Hyun W. Kim, Renuka Kadirvelraj, Charalampos Panagos, Neda Keyhaninejad, Maxwell Colonna, Pradeep Chopra, Dominic P. Byrne, Geert J. Boons, Esther van der Knaap, Patrick A. Eyers, Arthur S. Edison, Zachary A. Wood and Natarajan Kannan

Sci. Signal. **13** (639), eaax6313.
DOI: 10.1126/scisignal.aax6313

Kinase regulation conserved under stress

Oxidative stress is necessary for normal cellular function and tissue physiology but can also be pathological, and its effects are mediated in part through functional modification of various proteins. Shrestha *et al.* and Byrne *et al.* found that the oxidation of kinases at active site-adjacent cysteine residues, which were conserved across the eukaryotic kinome, regulated cell metabolism and mitosis. Shrestha *et al.* found that conserved cysteine residues within the diabetes-associated metabolic kinase FN3K acted as a toggle switch upon oxidation, promoting its functional oligomerization and consequently altering cellular redox status. Byrne *et al.* found that oxidation of mitotic kinases in human cells and yeast suppressed kinase catalytic activity and, in yeast, impaired cellular division. Exploring the effect of chronic oxidative stress on kinase function and how that may be spatiotemporally regulated may enable the development of new targeted therapeutics.

ARTICLE TOOLS

<http://stke.sciencemag.org/content/13/639/eaax6313>

SUPPLEMENTARY MATERIALS

<http://stke.sciencemag.org/content/suppl/2020/07/02/13.639.eaax6313.DC1>

RELATED CONTENT

<http://stke.sciencemag.org/content/sigtrans/13/615/eaay7315.full>
<http://stke.sciencemag.org/content/sigtrans/13/641/eabd8558.full>
<http://stke.sciencemag.org/content/sigtrans/13/641/eabb6707.full>

REFERENCES

This article cites 83 articles, 18 of which you can access for free
<http://stke.sciencemag.org/content/13/639/eaax6313#BIBL>

PERMISSIONS

<http://www.sciencemag.org/help/reprints-and-permissions>

Use of this article is subject to the [Terms of Service](#)

Science Signaling (ISSN 1937-9145) is published by the American Association for the Advancement of Science, 1200 New York Avenue NW, Washington, DC 20005. The title *Science Signaling* is a registered trademark of AAAS.

Copyright © 2020 The Authors, some rights reserved; exclusive licensee American Association for the Advancement of Science. No claim to original U.S. Government Works